

Autodetachment spectroscopy of metastable  $D_2^-$  and  $HD^-$ Raphaël Marion<sup>1,\*</sup>, Martin Čížek<sup>2</sup>, and Xavier Urbain<sup>1</sup><sup>1</sup>*Institute of Condensed Matter and Nanosciences, Université catholique de Louvain, B-1348 Louvain-la-Neuve, Belgium*<sup>2</sup>*Institute of Theoretical Physics, Faculty of Mathematics and Physics, Charles University in Prague, V Holešovičkách 2, 18000 Prague, Czech Republic* (Received 30 January 2023; accepted 26 April 2023; published 18 May 2023)

This paper reports observations of the autodetachment spectrum of  $D_2^-$  and  $HD^-$ , resolved in rovibrational levels presenting lifetimes from 1 to 100  $\mu$ s. The electronic kinetic-energy release was measured using the velocity-map imaging technique, enhanced by coincidence detection of the neutral species produced. The experimental results are compared with theoretical description of the *ab initio*-based nonlocal resonance model, confirming the main features predicted by theory while resolving the apparent discrepancy between spontaneous dissociation and detachment experiments by revealing the presence of an additional rovibrational level in  $D_2^-$  not predicted to be sufficiently long-lived by theory.

DOI: [10.1103/PhysRevA.107.052808](https://doi.org/10.1103/PhysRevA.107.052808)

## I. INTRODUCTION

The molecular anion  $H_2^-$  and its isotopologues are the most elementary negative molecules that we can find in the universe. With moderate rotational excitation, that structure has a really short lifetime (up to a few picoseconds), which allows us to consider it only as a resonant intermediate step in collisions, for example, the associative-detachment (AD) reaction:



While this reaction is believed to play a crucial role in first star formation [1] or as a benchmark for models of highly correlated, few-electron systems, the existence of long-lived metastable states (up to a microsecond or greater) has been a matter of debate both experimentally and theoretically. The first claims of direct observation date back to 1958 [2] and 1974 [3]. As some doubts about the reliability of the results have been raised, several experiments were conducted to test the statement, one contradicting this possibility [4] but many others supporting it [5–8]. Thanks to these mass-spectrometric observations, it is now definitively admitted that metastable states of these molecular anions exist.

Using an electrostatic ion-beam trap [9], multiple lifetimes have been observed, supporting additional predictions of the nonlocal model [10] which had already successfully described the dissociative-attachment reaction [11],



and, later on, quantitatively reproduced the cross section measured for the AD reaction (1) [12].

The picture that emerged for the underlying physics of long-lived states is sketched in Fig. 1, where the evolution of the effective potentials with the rotational excitation of

the anion is represented for the isotopologue  $D_2^-$ . Note that the violet lines represent the part of the potential where the anion is unstable against autodetachment and cannot support a long-lived metastable state. For a sufficiently high angular momentum  $J$ , the centrifugal distortion of the potential-energy curve, i.e.,

$$V_{\text{eff}} = U(R) + \frac{\hbar^2 J(J+1)}{2\mu R^2}, \quad (3)$$

leads to the formation of an external well, strongly suppressing autodetachment toward the potential well of the neutral molecule. This outer region hosts long-lived rovibrational states that can decay by tunneling into  $D + D^-$  or by detaching into  $D_2 + e^-$  through the inner barrier.

The first experimental investigation of rovibrational states based on photofragment imaging [13] confirmed the theoretical interpretation of experimental lifetime measurements but also called for deep theoretical improvements. However, further analysis based on foil-induced Coulomb explosion imaging [14,15] instead consolidated the theoretical model. Photodetachment of  $H_2^-$  was also considered both theoretically [16] and experimentally [17,18], exhibiting unexpected oscillations in cross sections that are still under investigation.

More recently, we measured the kinetic-energy release of  $D$  and  $D^-$  fragments produced by spontaneous dissociation of  $D_2^-$  [19]. A single value for the resonant energy relative to the dissociation limit was found at  $22.8 \pm 0.3$  meV, which could not be assigned to any predicted long-lived rovibrational state, reviving the need to explore more deeply the quantum structure of this molecular anion.

To date, no experiments have been conducted by measuring the spontaneous detachment of electrons from the anions. The present work fills this gap, providing, with high resolution, a direct measurement of energy levels and angular momentum of the rovibrational states of  $D_2^-$  and  $HD^-$  as well as the

\*raphael.marion@uclouvain.be

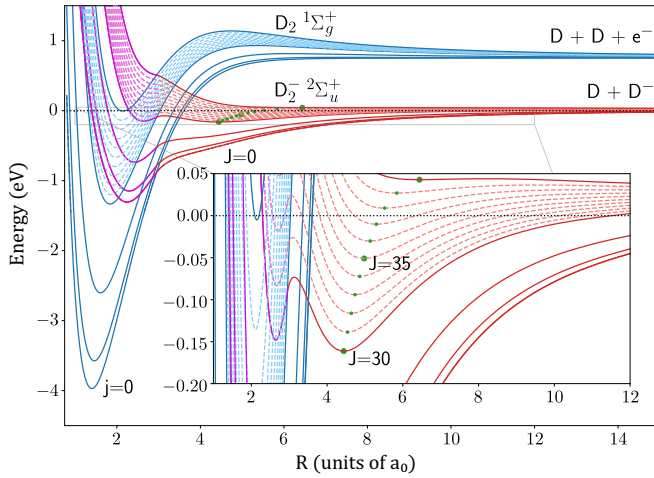


FIG. 1. Potential-energy curves for different  $J$  levels (red lines turning violet in the autodetachment region) of  $D_2^-$  and  $j$  levels (blue lines) of  $D_2$ . Dashed lines show levels between  $J = 30$  and  $J = 40$ , and solid lines show  $J$  in multiples of 10, while others are not represented for the sake of readability. The black dotted line corresponds to the dissociation limit of  $D_2^-$ , and the green circles indicate the location of the minima in the outer region.

branching ratios between the various channels involved in the dynamics of the autodetachment process.

The structure of the paper is as follows: the experimental method and data analysis used to determine the autodetachment spectrum are described in Sec. II; Sec. III presents the *ab initio* methods used for calculations. The results and their interpretation are detailed and discussed in Sec. IV. The conclusions and perspectives for future work are presented in Sec. V.

## II. EXPERIMENT

### A. Experimental setup

As sketched in Fig. 2, negative molecular beams are produced in a duoplasmatron source, lifted at a potential of 3 kV and filled with pure  $D_2$  gas for the production of  $D_2^-$  or with a 1:1 mixture of  $D_2$  and  $H_2$  gas for the production of  $HD^-$ . A permanent magnet performs a mass selection, and the cleaned and collimated beam is guided by electrostatic optics to the velocity-map imaging (VMI) spectrometer [20,21], where the spontaneously detached electrons are extracted perpendicularly by an electrostatic plate and directed through a combination of electrostatic lenses. The repeller electrode is split to correct the trajectory of the anions by applying a slightly different bias at both the entrance and exit, maintaining a horizontal trajectory of the neutrals produced inside the spectrometer. Electrons are detected using a detection system correlating the brightness of the light spots with the amplitude of the electrical signals in order to retrieve the timing information (COBRA) [22]. It consists of three stacked microchannel plates (MCPs), a phosphor screen, a complementary metal-oxide semiconductor (CMOS) camera, and a wave-form digitizer.

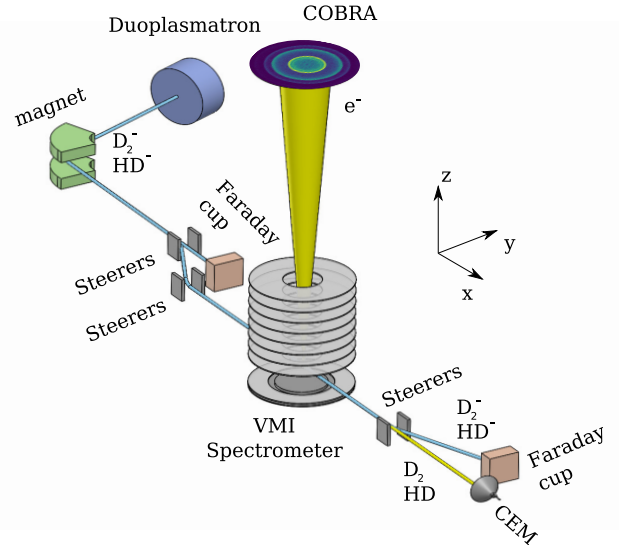


FIG. 2. Experimental setup.

The first images obtained with that setup showed strong blurring in the direction of propagation of the beam as the detachment process may occur everywhere along the path through the spectrometer. As the principle of the VMI technique is to achieve a Fourier transform of the transverse velocity (parallel to the focal plane) by placing a position sensitive detector at the focal plane of the electrostatic lens, the imaging of an ideal spectrometer should be independent of the emission point. However, in practice, it is true for only a limited spatial extent, and as a result, small variations in the imaging process of identical transverse velocities may be observed for significantly different emission points.

Taking advantage of the low beam current, implying that the quantity of emitted electrons is so low that they can be detected one by one, we installed in a straight line a channel electron multiplier (CEM) with high detection efficiency behind the VMI spectrometer and after steerers which deviate the residual anions. We synchronized the pulses, one appearing when an electron hits the MCPs and another one appearing when a neutral molecule hits the CEM, by delaying the signal of electron detection by a duration equal to the time of flight (TOF) of a neutral molecule from the center of the VMI spectrometer to the CEM.

Keeping only the events detected in coincidence, we were able to classify each of them according to the precise position where the autodetachment occurred inside the spectrometer. The time window used for the coincidence was set to be long enough to neglect any imprecisions in the estimated delay but short enough to prevent the detection of autodetachment events along the same straight line but outside the VMI. For the events that passed the test, a greater precision ( $\sim 1$  ns) was achieved by recording precisely the elapsed time between the detections of the two validated hits.

Considering only small subsets of events together, corresponding to small regions of emission, we then applied our usual procedure [20,21] to compensate magnetic-field inhomogeneities and aberrations of the lenses in order to recover the circular shape of the distribution of events. We refocused and scaled to the same magnification each time slice of the

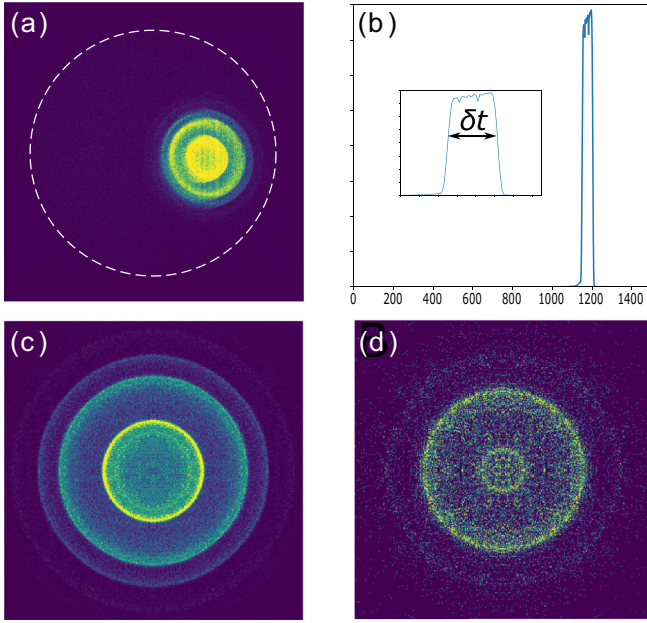


FIG. 3. Data preprocessing: (a) Raw picture obtained for  $D_2^-$ . The dashed circle indicates the edge of the detection area (80 mm in diameter). (b) Recorded delays (in ns) between electron and neutral detection for  $D_2^-$ . (c) Processed distribution for  $D_2^-$ . (d) Processed distribution for  $HD^-$ .

distribution to recover sharpness in the final image. A picture of the raw and processed images, as well as the recording of the TOF, is presented in Fig. 3.

### B. Data analysis

To extract information from the distribution of events, an Abel inversion must be performed as the observed picture is the projection of Newton spheres growing proportionally with the radial velocity expressed in a moving frame passing through the lenses of the spectrometer, associated with the spherical distribution of electrons emitted at well-defined energies. A first-order calibration of the energy scale is obtained by recording the photodetachment spectrum of an anion with well-known electronic affinity (e.g.,  $H^-$ ,  $C^-$ , or  $O^-$ ).

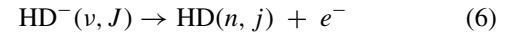
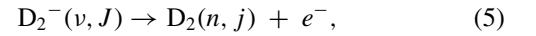
To proceed with the image analysis, we previously used the maximum entropy velocity Legendre reconstruction (MEVELER) algorithm [23], generally preferred to PBASEX [24] as it avoids mathematical inversion of this ill-conditioned problem by solving it in a Bayesian framework instead of relying on matrix inversions. This makes the solution more robust by avoiding the appearance of artifacts in the inverted distribution. However, MEVELER and the other usual methods do not estimate the physical parameters involved in the process but achieve a nonparametric estimation of a more flexible “free-form” solution. The onus of parameter extraction as well as the evaluation of uncertainties is therefore shifted on the user, a tractable task for well-separated peaks in the radial distribution that becomes rapidly unreliable when the separations are not sharp enough, situations frequently encountered when many channels are involved. For these reasons, while these algorithms are able and essential to unveil the main features

of the dynamics at play, we have limited ourselves in their use to furnishing reasonable priors allowing more in-depth analysis.

Staying in a Bayesian framework, the task is to extract knowledge about unknown values of the different parameters  $X \equiv \{X\}$ , knowing the distribution of observed events  $D \equiv \{D\}$  interpreted in a particular model  $M$  accounting for possible observable transitions in our system, completed by the available background information  $I$ . This evaluation is given by the so-called *posterior* probabilities  $\Pr(X|DMI)$  that can be computed by application of Bayes’s theorem:

$$\Pr(X|DMI) = \frac{\Pr(D|XMI) \Pr(X|MI)}{\Pr(D|MI)}. \quad (4)$$

The background information  $I$  about the reactions



includes the following facts and observations:

(i) No angular dependence is observed in the data  $\{D\}$  because of the random orientation of the molecular anions in the laboratory frame, allowing the reduction to only a radial analysis.

(ii) The relative spacing between energies of released electrons from a specific rovibrational state of the anion, labeled  $(\nu, J)$ , decaying to a set of different rovibrational states of the neutral, labeled  $(n, j)$ , depends only on the internal structure of the neutral. The absolute position of that set in the spectrum still requires the determination of the energy  $E_{\nu J, n_0 j_0}$  of one of the transitions originating from the same initial state (we have selected the one with the highest branching ratio), but the others are related to it by the rovibrational spacings  $\Delta e_{nj, n_0 j_0}$  that are known [25] with such great precision that we can consider them to be constants and use them as an intrinsic ruler, extending the accuracy obtained by the absolute calibration. It is formalized by a parameter  $\alpha$  such that each transition forming a particular Newton sphere of radius  $r_{\nu J, nj}$  corresponds to an energetic level given by

$$\begin{aligned} r_{\nu J, nj} &= \alpha \sqrt{E_{\nu J, nj}}, \\ E_{\nu J, nj} &= E_{\nu J, n_0 j_0} + \Delta e_{nj, n_0 j_0}. \end{aligned} \quad (7)$$

(iii) Gerade-ungerade inversion symmetries impose selection rules between the angular momentum  $j$  of the neutral molecule and the angular momentum  $J$  of the molecular anion. More details are given in Sec. III that justify that the only significant transitions follow the  $j = J \pm 1$  selection rules.

(iv) Resolution of the spectrometer is the same for all channels and can be modeled by the convolution with a normalized Gaussian characterized by a standard deviation  $\sigma$  corresponding to the point spread function of the VMI.

(v) The statistics associated with each radial bin  $\Delta r$ , in which  $D_r = D(r)\Delta r$  events are observed, is Poissonian, with a parameter corresponding to the sum of a small uniform background  $b$  and a variable signal  $s_r = s(r)\Delta r$ . The *likelihood* function is then given by

$$\Pr(D|XMI) = \prod_r \frac{(b + s_r)^{D_r} e^{-(b+s_r)}}{D_r!}, \quad (8)$$

where  $s(r)$  is the local Abel projection of a sum of Newton spheres spread by the VMI spectrometer and associated with each decay channel, given by

$$s(r) = \sum_{v,J} \sum_{n,j} A_{vJ,nj} S_{vJ,nj}(r),$$

$$S_{vJ,nj}(r) = 2\pi r \int_r^{+\infty} \frac{e^{-\frac{(\rho-r_{vJ,nj})^2}{2\sigma^2}}}{4\pi \rho^2 \sqrt{2\pi} \sigma} \frac{2\rho d\rho}{\sqrt{\rho^2 - r^2}}$$

$$= \int_r^{+\infty} \frac{e^{-\frac{(\rho-r_{vJ,nj})^2}{2\sigma^2}}}{\sqrt{2\pi} \sigma} \frac{r d\rho}{\rho \sqrt{\rho^2 - r^2}}. \quad (9)$$

The parameters to be estimated are  $X = \{\{A_{vJ,nj}\}, \{E_{vJ,n_0j_0}\}, b, \alpha, \sigma\}$ , with  $A_{vJ,nj}$  defined as the respective weight of a given channel. The *prior* probabilities  $\Pr(X|MI)$  must impose that all of these parameters are positive and have a proper definition to allow model comparison. We also desire to take into account the insights provided by the free-form algorithms while remaining sufficiently open-minded to reflect to a high extent our lack of knowledge before experiments. In place of a sharp-edged broad uniform probability, raising some numerical difficulties in the treatment of the discontinuities, we have chosen to use the smoother gamma distributions

$$\mathcal{G}(X_i; k_i, \theta_i) = \frac{1}{\Gamma(k_i)\theta_i^{k_i}} X_i^{k_i-1} e^{-\frac{X_i}{\theta_i}}, \quad (10)$$

where  $k_i$  and  $\theta_i$  are selected to produce maxima corresponding to the qualitative estimates based on the free-form solution and to a standard deviation of 75% of these values.

As there are about 20 parameters to refine (depending on the analysis model  $M_i$  using different numbers of initial states), a brute-force approach to compute the posterior probability is not adapted. Instead, we have used an iterative procedure to maximize the log-posterior function  $P(X) = \ln[\Pr(X|DMI)]$  by a simple Newton-Raphson-type procedure (sometimes simply called *natural gradient descent*) requiring the computation of the gradient  $\nabla P(X)$  and the Hessian matrix  $\nabla \nabla P(X)$ :

$$X_{n+1} = X_n - [\nabla \nabla P(X_n)]^{-1} \nabla P(X_n). \quad (11)$$

The optimal parameters  $\{X_{\text{opt}}\}$  are obtained when  $\nabla P(X_{\text{opt}}) = 0$ , and their precision is given by  $\text{Var}[X]$ , the variance extracted from the diagonal of the variance-covariance matrix  $\Sigma = -[\nabla \nabla P(X_{\text{opt}})]^{-1}$ , according to a second-order development around the maximum of  $P(X_{\text{opt}})$  equivalent to a multivariate Gaussian approximation of posterior probability.

In that approximation, the computation of the *evidence* associated with a specific model  $M$  is direct and given for  $N_M$  optimal parameters  $X_M = \{X_{\text{opt}}\}$  by

$$\Pr(D|MI) = \int \Pr(D|XMI) \Pr(X|MI) d^M X$$

$$= \sqrt{(2\pi)^{N_M} \det(\Sigma_M)} e^{P(X_M)}. \quad (12)$$

The comparison between two models is conducted naturally by computing the odds:

$$\frac{\Pr(M_1|DI)}{\Pr(M_2|DI)} = \frac{\Pr(D|M_1I) \Pr(M_1|I)}{\Pr(D|M_2I) \Pr(M_2|I)}$$

$$\approx \frac{\Pr(D|M_1I)}{\Pr(D|M_2I)} \equiv B_{12}, \quad (13)$$

where the factor  $\frac{\Pr(M_1|I)}{\Pr(M_2|I)}$  is taken to be equal to 1 as no preference is given to one model or the other, while  $B_{12}$  is called the *Bayes factor*, which favors model  $M_1$  when  $B_{12} > 1$ . It is good to note here that the *evidence* includes the goodness of fit to the data of a model thanks to the presence of the likelihood quantity but also penalizes the complexity of a model, which increases with the number of unknown parameters. This feature is usually recognized as acting like *Occam's razor* [26], also known as *principle of parsimony*.

The energy levels of the molecular anions, referenced to the dissociation limit, can be extracted knowing the energy levels relative to the dissociation limit of the neutral target  $E_{n_0j_0}$  [25] and the electronic affinities  $EA_{\text{H}}$  and  $EA_{\text{D}}$  of hydrogen and deuterium. For  $\text{D}_2^-$  we used the value  $EA_{\text{D}} = 754.656$  meV given in [27], and for  $\text{HD}^-$  we used the mean of  $EA_{\text{D}}$  and  $EA_{\text{H}} = 754.208$  meV from the same reference, both given with uncertainties far smaller than experimental ones. Supplementary uncertainty is added to take into account the effect of preprocessing data, which is of the order of  $\Delta r$ :

$$E_{\text{D}_2^-}(v, J) = E_{\text{D}_2}(n_0, j_0) - EA_{\text{D}} - E_{vJ,n_0j_0},$$

$$\text{Var}[E_{\text{D}_2^-}(v, J)] = \text{Var}[E_{vJ,n_0j_0}] + \left(2 \frac{r_{vJ,n_0j_0}}{\alpha^2} \Delta r\right)^2. \quad (14)$$

The branching ratios are considered to be the proportion of events starting from one specific state  $(v, J)$  to all possible target states  $(n, j)$ . From the estimated parameter, they are given by

$$B_{vJ,nj} = \frac{A_{vJ,nj}}{\sum_{n'j'} A_{vJ,n'j'}} \equiv \frac{A_{vJ,nj}}{N_{vJ}},$$

$$\text{Var}[B_{vJ,nj}] = \sum_{n'j'} \sum_{n''j''} \frac{\partial B_{vJ,nj}}{\partial A_{vJ,n'j'}} \frac{\partial B_{vJ,nj}}{\partial A_{vJ,n''j''}}$$

$$\times \text{Cov}(A_{vJ,n'j'}, A_{vJ,n''j''}),$$

$$\frac{\partial B_{vJ,nj}}{\partial A_{vJ,n'j'}} = \frac{N_{vJ} \delta_{nj,n'j'} - A_{vJ,nj}}{N_{vJ}^2}. \quad (15)$$

Finally, from the relative weights of the different channels, we can extract approximate constraints on the lifetime of certain states of the anions. Indeed, our observations access only a limited number of initial states that present lifetimes compatible with our setup, depending on the combined efficiency of dissociation (D) and autodetachment (A) processes. For a state with lifetime  $\tau_{vJ} = (\Gamma_{vJ}^{(\text{A})} + \Gamma_{vJ}^{(\text{D})})^{-1}$  that enters the spectrometer after a time flight  $t_{\text{in}}$  and leaves it at  $t_{\text{out}} = t_{\text{in}} + \delta t$ , as represented in Fig. 3, the number of detected events  $N_{vJ} = \sum_{n,j} A_{vJ,nj}$  is related to the initial population  $p_{vJ}$  by

$$N_{vJ} = \beta_{vJ} \gamma_{vJ} p_{vJ},$$

$$\gamma_{vJ} = e^{-t_{\text{in}}/\tau_{vJ}} - e^{-t_{\text{out}}/\tau_{vJ}} \approx e^{-t_{\text{in}}/\tau_{vJ}} \delta t / \tau_{vJ},$$

$$\beta_{vJ} = \frac{\Gamma_{vJ}^{(\text{A})}}{\Gamma_{vJ}^{(\text{A})} + \Gamma_{vJ}^{(\text{D})}}, \quad (16)$$

where  $\Gamma_{\nu J}^{(A)}$  and  $\Gamma_{\nu J}^{(D)}$  are the autodetachment and dissociation rates of state  $(\nu, J)$ , respectively. The approximate functional form of the observability factor  $\gamma_{\nu J} = \gamma(\tau_{\nu J})$  illustrates two competing effects of the lifetime on the detection rate. A long lifetime implies that a significant proportion of anions in that specific state will survive until it reaches the spectrometer, while a too long lifetime, compared to the transit time through the spectrometer, will produce a rate below detectability. The autodetachment branching ratio  $\beta_{\nu J}$  accounts for the possibility of dissociation via tunneling through the long-range barrier.

Assuming a Maxwell-Boltzmann distribution of the rovibrational levels for a source at temperature  $T \in [2000 \text{ K}, 4000 \text{ K}]$ , one may expect a detected fraction given by

$$\frac{N_{\nu J}}{\sum_{\nu' J'} N_{\nu' J'}} = \frac{(2J+1)\beta_{\nu J}\gamma_{\nu J}e^{-E_{\nu J}/k_B T}}{\sum_{\nu' J'} (2J'+1)\beta_{\nu' J'}\gamma_{\nu' J'}e^{-E_{\nu' J'}/k_B T}}. \quad (17)$$

With the experimental values obtained by Heber *et al.* [9] and based on an estimation of time of flight  $t_{\text{in}}$  and the transit time  $\delta t$  through the spectrometer ( $\sim 20 \text{ ns}$ ), our experimental values provide complementary parameters allowing estimation of missing lifetimes. To evaluate uncertainties, we vary all the uncontrolled parameters across the interval of possible values and take the resulting variations as standard deviations, of which we take the quadratic sum. Because of these unknowns, however, we insist that these values are not obtained from an experiment designed to measure lifetimes, like an ion trap, and invite the reader to keep in mind that they are just given in Sec. IV as a rough estimation of their magnitude.

### III. THEORY

To describe the dynamics of the  $\text{H}_2^-$  system we use the discrete-state-in-continuum representation to parametrize the interaction of electronic metastable states with the electron continuum. This approach was developed in 1960s (see, for example, [28,29] and references therein) for the description of both electron-molecule and anion-atom collisions. In 1980, Bieniek [30] pointed out the need to use the full nonlocal version of the theory to describe correctly the ratio of the individual  $\text{H}_2(n, j) + e^-$  channels in the decay of the  $\text{H}_2^-$  complex formed by  $\text{H} + \text{H}^-$  collisions. We developed the nonlocal model of the  $\text{H}_2^-$  collision complex in 1998 [31] based on previous projection-operator decomposition of the electron dynamics to the discrete state and the continuum [32] and an accurate potential-energy curve for the anion bound state [33]. We used this model to calculate the associative detachment [12,31,34,35], dissociative attachment [11], and vibrational excitation [36] and also to predict the properties of the long-lived anion states [10]. We summarized the theory and some results in two chapters in [37].

The central equation of the current approach (see, for example, [38,39]) is the Schrödinger equation for the projection of the complete wave function of the  $\text{H}_2^-$  scattering complex on the electronic discrete state. After partial wave expansion

this equation reads

$$\left( -\frac{1}{2\mu} \frac{d^2}{dR^2} + V_d(R) + \frac{J(J+1)}{2\mu R^2} + F_J \right) \psi_J(R) = E \psi_J(R), \quad (18)$$

where  $V_d(R)$  is the discrete-state (anion) potential and  $F_J$  is the nonlocal potential accounting for the coupling of the discrete state to the continuum of the departing electrons with momentum  $k$  through the coupling matrix element  $V_{dk}$ :

$$F_J \psi_J(R) = \int dR' \int k dk V_{dk}(R) f_J \left( E - \frac{1}{2}k^2, R, R' \right) \times V_{dk}^*(R') \psi_J(R). \quad (19)$$

The quantity  $f_J(E', R, R')$  describes the neutral molecule after the electron has left [30]:

$$f_J(E', R, R') = \frac{J+1}{2J+1} g_{J+1}(E', R, R') + \frac{J}{2J+1} g_{J-1}(E', R, R'), \quad (20)$$

and it is given by the weighted average of the Green's function for radial nuclear motion of the neutral molecule

$$g_j(E', R, R') = \langle R | \left( E' + \frac{1}{2\mu} \frac{d^2}{dR^2} - V_0(R) - \frac{j(j+1)}{2\mu R^2} + i\varepsilon \right)^{-1} | R' \rangle = \sum_n \chi_n^j(R) \frac{1}{E' - E_n^j + i\varepsilon} \chi_n^j(R') \quad (21)$$

for two possible angular momenta,  $j = J - 1$  and  $j = J + 1$ . The effective nonlocal potential (19) thus describes how the motion of the anion in the potential  $V_d(R)$  is influenced by decay into states  $|\chi_n^j\rangle$  bound in the neutral molecular potential  $V_0(R)$ . The form of Eq. (20) reflects the conservation of angular momentum [40], taking into account only the lowest partial wave ( $p$  wave) of the electron allowed by the symmetry of the charge distribution [41]. For a larger change in angular momentum the coupling element is suppressed by one order of magnitude [32]. In our previous work on the decay of the molecular hydrogen anion [10] we neglected this change in angular momentum and used the following approximation:

$$f_J(E', R, R') = \frac{J+1}{2J+1} g_{J+1}(E', R, R') + \frac{J}{2J+1} g_{J-1}(E', R, R') \simeq g_J(E', R, R'), \quad (22)$$

replacing the weighted average action of the Green's functions for a molecule with angular momenta  $J + 1$  and  $J - 1$  by the single action of the Green's function with angular momentum  $J$ . While this approximation does not have a big influence on integral quantities like the total associative-detachment rates and lifetime of the metastable states, it does not allow the calculation of the correct ratios of the decay channels of the metastable anion into all final molecular states since the correct molecular states are not even present in the description. In the present work we keep the full form (20).

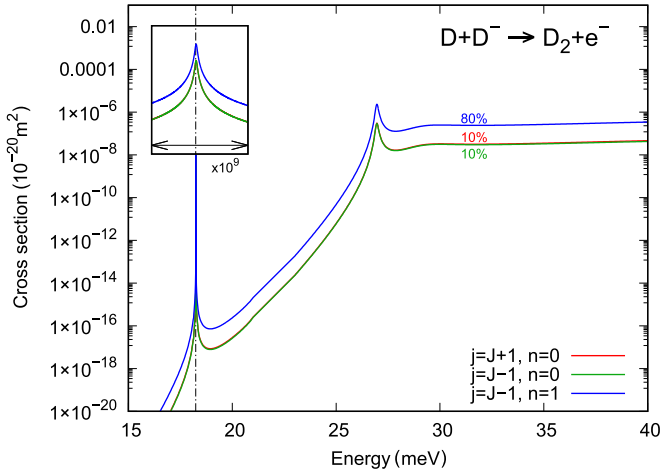
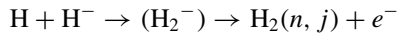


FIG. 4. Contribution of partial wave  $J = 37$  to the associative detachment  $D + D^- \rightarrow D_2(n, j) + e^-$  cross section with different final rovibrational states  $j$  and  $n$ . The inset shows the  $(\nu = 1, J = 37)$  resonance with the energy scale expanded by nine orders of magnitude (the y axis in the inset is to scale).

To determine the ratio of the individual decay channels we analyzed the cross sections for the AD processes of  $H_2^-$  and its isotopologues



for individual final states  $(n, j)$  close to known [10] anion resonances  $H_2^-(\nu, J)$ . As an example for  $D_2^-$ , Fig. 4 shows the partial wave  $J = 37$  contribution to low-energy cross sections of this process for three different final states. The final states involved and the resonance states are shown in Fig. 5. First observe that the cross section is, in general, increasing up to an energy of 27 meV (height of the outer barrier above the

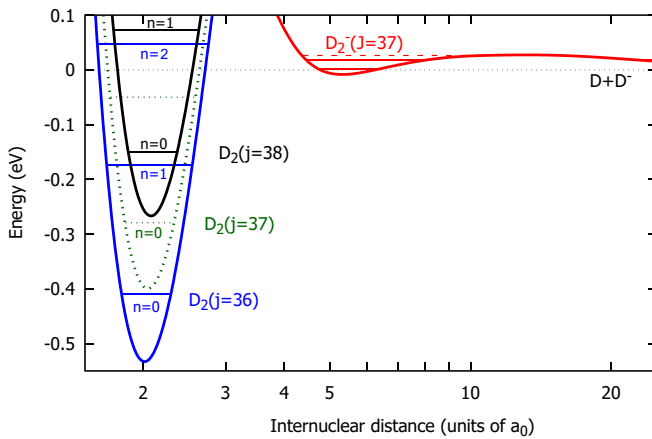


FIG. 5. Potential curves and levels (red lines) relevant for  $D_2^-$  with angular momentum  $J = 37$ . Dominant decay channels are shown. They involve dissociation to  $D^- + D$  (dotted line) and autodetachment to rovibrational states of neutral molecule (blue and black lines). Autodetachment to  $j = 37$  (green dashed line) is forbidden by parity conservation. Notice that logarithmic scale is used for internuclear distance to facilitate viewing neutral and anion potentials with different length scales simultaneously.  $\nu = 2$  resonance with too short lifetime is shown by the red dashed line.

$D + D^-$  dissociation threshold), and then it becomes rather flat. On top of this behavior, we can see two resonances. One rather weak and broad at  $E = 27$  meV comes from state  $(\nu = 2, J = 37)$ , which is (for the current model) too close to the top of the barrier and has a too short lifetime (approximately picoseconds) to be detectable. A more dramatic resonance  $(\nu = 1, J = 37)$  manifests as a very narrow peak near 18 meV and has a predicted lifetime of 16  $\mu$ s. The other resonance,  $(\nu = 0, J = 37)$ , is not seen in the graph since it is located in the region close to zero energy with the cross-section magnitude below  $10^{-65} \text{ m}^2$ , but we still have clear cross sections to analyze the resonance width and its decay channels.

We assume that the associative detachment process at low energies proceeds in two steps. The first step is an attachment to the resonance state by tunneling through the outer barrier. The second step is tunneling through the inner barrier while simultaneously releasing an electron. The first step determines the overall shape of the associative detachment cross-section curve, while the second is decisive for the ratio of the cross section for each individual final channel. For  $J = 37$  we have three accessible final states over the whole energy region shown in Fig. 4. We observe that the ratio (the number written close to each line) of the cross sections for all individual channels is fairly constant throughout the energy range. In particular for an energy close to the resonance energy, the ratio of the individual final channels in the associative detachment process is identical to the ratio of the individual final channels in the decay of the metastable anion state.

To understand the resulting ratios we should remember that the AD cross sections (and also the ratios of the autodetachment-decay channels) are proportional to

$$|\langle \chi_n^j | V_{dk}(R) | \psi_J \rangle|^2.$$

The functions  $\langle R | \psi_J \rangle$  and  $\langle R | \chi_n^j \rangle$  are obtained by solving the Schrödinger equation with the potentials  $V_d(R) + F$  and  $V_0(R)$  of the anion and neutral molecule, including the centrifugal term. The decay-channel ratios are thus proportional to the overlap of the functions  $\langle R | \psi_J \rangle$  and  $\langle R | \chi_n^j \rangle$  modified by the discrete-state continuum coupling element  $V_{dk}$ . The  $R$  dependence of this element is weaker than the  $R$  dependences of the wave functions, which overlap by tunneling tails. But the dependence of  $V_{dk}$  on the energy of the released electron  $\epsilon = \frac{1}{2}k^2 = E - E_n^j$  is important if  $\epsilon$  is small since the threshold behavior of the coupling is, according to Wigner's threshold law for  $p$  electron ejection,

$$V_{dk}(R) \sim k^3 \sim \epsilon^{3/2}, \quad \epsilon \rightarrow 0;$$

that is, the channels releasing the electron with small energy will be suppressed. We also analyzed the cross sections for  $J = 36$  for  $D + D^-$  and  $J = 30, 31$  for  $H + D^-$  similarly to the data in Fig. 4 to get the data for all states shown in the tables below.

#### IV. RESULTS AND DISCUSSIONS

In Figs. 6 and 7, we present the experimental radial distributions as well as their analysis for reactions (5) and (6), respectively. The top graphs show our best fit to the data, composed of the projection of the individual Newton spheres

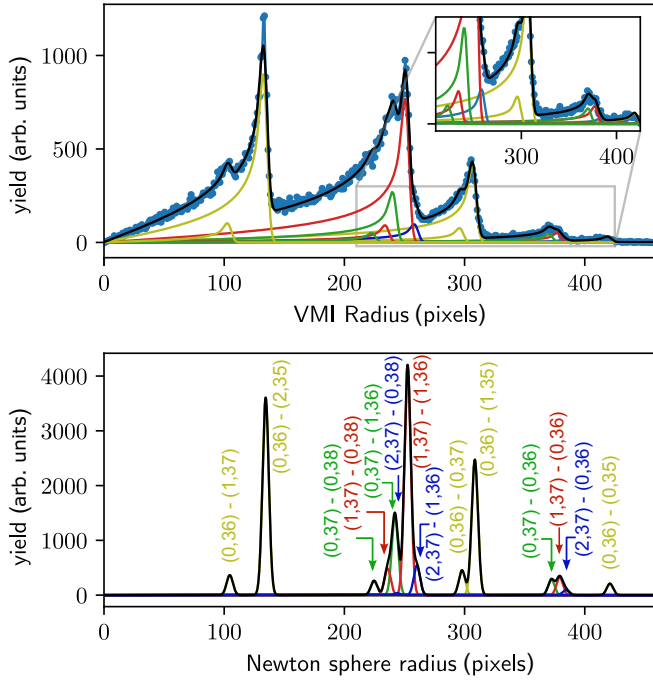


FIG. 6. Best fit of experimental data (top) and posterior estimation of Abel inversion (bottom) obtained for autodetachment of  $D_2^-$ , reaction (5). Colors correspond to the same transitions in both plots.

corresponding to each channel convoluted with the point spread function of the VMI, in black; all transitions starting from the same initial state are shown in the same color. The bottom graphs show the reconstructed radial distribution after

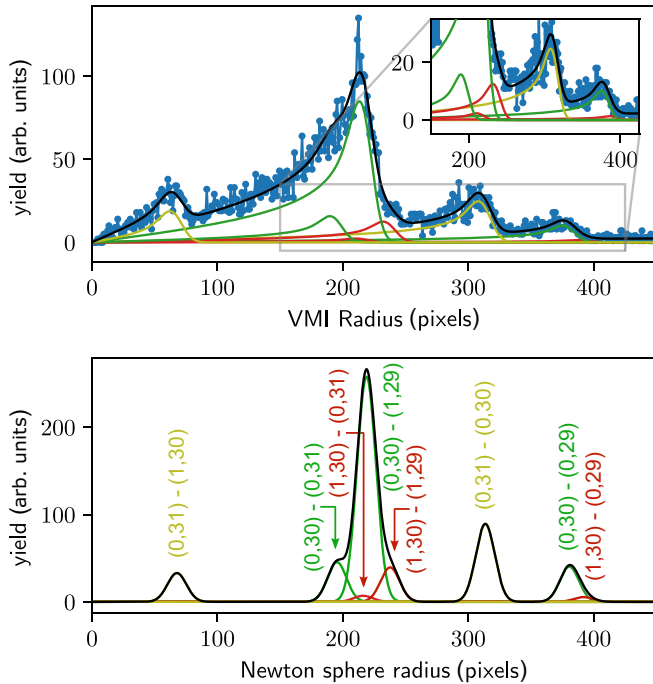


FIG. 7. Best fit of the experimental data (top) and posterior estimation of Abel inversion (bottom) obtained for autodetachment of  $HD^-$ , reaction (6). Colors correspond to the same transitions in both plots.

TABLE I. Experimental and theoretical (in italics) kinetic energy (in meV) of released electrons for rovibrational states of  $D_2^-$  accessible to our experiment.

$(n, j) \swarrow (v, J)$	(0,36)	(0,37)	(1,37)	(2,37)
$(0, J + 1)$	261.8	148.9	164.6	177
	263	<i>152</i>	<i>168</i>	<i>177</i>
$(1, J + 1)$	32.3	–	–	–
	<i>34</i>			
$(0, J - 1)$	522.8	408.6	424.4	436.7
	524	<i>412</i>	<i>428</i>	<i>437</i>
$(1, J - 1)$	280.9	172.8	188.6	200.9
	282	<i>176</i>	<i>192</i>	<i>201</i>
$(2, J - 1)$	53.4	–	–	–
	<i>55</i>			
Expt. uncertainty				
Fit	$\pm 0.04$	$\pm 0.28$	$\pm 0.08$	$\pm 0.53$
Preprocessing	$\pm 0.8$	$\pm 1.4$	$\pm 1.5$	$\pm 1.5$
Total	$\pm 0.8$	$\pm 1.4$	$\pm 1.5$	$\pm 1.6$

Abel inversion (Newton sphere), with the colors following the same pattern.

In Tables I and II, we compare quantitatively the energy measured and predicted for detached electrons in each channel of  $D_2^-$  and  $HD^-$ , respectively. These theoretical energies and the branching ratios, compared to experimental values in Tables III and IV for  $D_2^-$  and  $HD^-$ , respectively, were extracted from AD cross-section data similar to Fig. 4. As explained in Sec. II, the uncertainties are the same for all decays from identical channels as they are mutually linked by common  $(n_0, j_0)$  levels of neutral molecules that are known with high precision.

Observing the data in Tables III and IV, we notice that where no threshold effect is expected, the vibrational quantum number  $n$  of the neutral molecule is the most decisive factor for the importance of that particular decay channel. For example the  $(v, J) = (0, 37)$  resonance can decay into three channels,  $(n, j) = (0, 38)$ ,  $(0, 36)$ , and  $(1, 36)$ . The last of the channels, which is the only one with vibrational quantum number  $n = 1$ , is the most important. Note that the calculated decay channels do not include the dissociation channel

TABLE II. Experimental and theoretical (in italics) kinetic energy (in meV) of released electrons for rovibrational states of  $HD^-$  accessible to our experiment.

$(n, j) \swarrow (v, J)$	(0,30)	(1,30)	(0,31)
$(0, J + 1)$	113.18	138.63	–
	<i>117</i>	<i>135</i>	
$(0, J - 1)$	429.71	455.16	291.74
	<i>434</i>	<i>452</i>	<i>295</i>
$(1, J - 1)$	142.13	167.58	13.59
	<i>146</i>	<i>164</i>	<i>17</i>
Expt. uncertainty			
Fit	$\pm 0.41$	$\pm 1.85$	$\pm 0.25$
Preprocessing	$\pm 1.3$	$\pm 1.4$	$\pm 1.5$
Total	$\pm 1.4$	$\pm 2.3$	$\pm 1.5$

TABLE III. Experimental and theoretical (in italics) branching ratios (in percent) for autodetachment channels from rovibrational states of  $D_2^-$  accessible to our experiment.

$(n, j) \setminus (v, J)$	(0,36)	(0,37)	(1,37)	(2,37)
$(0, J + 1)$	$7 \pm 1$ <i>4</i>	$10 \pm 4$ <i>10</i>	$6 \pm 3$ <i>10</i>	$6 \pm 5$ <i>10</i>
$(1, J + 1)$	$5 \pm 1$ <i>11</i>	–	–	–
$(0, J - 1)$	$3 \pm 0.5$ <i>3</i>	$11 \pm 2$ <i>10</i>	$8 \pm 1$ <i>10</i>	$12 \pm 4$ <i>10</i>
$(1, J - 1)$	$35 \pm 1$ <i>27</i>	$79 \pm 4$ <i>80</i>	$86 \pm 3$ <i>80</i>	$82 \pm 7$ <i>80</i>
$(2, J - 1)$	$50 \pm 0.5$ <i>54</i>	–	–	–

$D + D^-$  when their energy lies above the dissociation limit. The calculation of the partial widths of these channels toward dissociation is difficult since they are governed by tunneling through a very thick potential-energy barrier. The tunneling rate is thus exponentially sensitive to the exact shape of the potential-energy curve at long range. We decided not to include the data for this process since this channel is negligible for most of the resonances studied here. The theoretical numbers in Tables III and IV thus give the relative importance of only the individual autodetachment channels.

The data tables for the decay of  $HD^-$  states are shorter since the lighter system accommodates fewer metastable states. While the branching ratios for resonances with  $J = 30$  in  $HD^-$  look similar to those for  $J = 37$  in  $D_2^-$ , the last column of the Table IV for  $J = 31$  looks qualitatively different. In this case the ground vibrational state  $(n, j) = (0, 30)$  is preferred over the excited  $(1, 30)$  state. The reason for this inverted ratio is the above-mentioned threshold effect inducing  $\epsilon$  dependence in the coupling element  $V_{dk}$ . The reduction of the  $(0, 31) \rightarrow (1, 30)$  channel due to small electron energy ( $\sim 15$  meV) prevails over the enhancement due to the more extended vibrational wave function of the excited state.

Extracted from these analyses, the new benchmark values for energy levels and lifetimes for  $D_2^-$  and  $HD^-$  are summarized in Tables V and VI respectively. For both anions, only a few rovibrational states are present in the tables because they are limited to those observable with the present configuration of our experimental setup, following the observability curve  $\gamma_{v,J}$  introduced in Sec. II. Those are given in Fig. 8 with a

TABLE IV. Experimental and theoretical (in italics) branching ratios (in percent) for autodetachment channels from rovibrational states of  $HD^-$  accessible to our experiment.

$(n, j) \setminus (v, J)$	(0,30)	(1,30)	(0,31)
$(0, J + 1)$	$13 \pm 2$ <i>10</i>	$13 \pm 11$ <i>11</i>	–
$(0, J - 1)$	$12 \pm 1$ <i>15</i>	$10 \pm 6$ <i>15</i>	$73 \pm 2$ <i>69</i>
$(1, J - 1)$	$75 \pm 2$ <i>76</i>	$77 \pm 11$ <i>74</i>	$27 \pm 2$ <i>31</i>

TABLE V. Experimental and theoretical (in italics) [10] lifetime and energy level referred to the dissociation asymptote ( $D + D^-$ ) for experimentally accessible rovibrational states of  $D_2^-$ .

$(v, J)$	$\tau_{\text{exp}}$ ( $\mu\text{s}$ )	$\tau_{\text{th}}$ ( $\mu\text{s}$ )	$E_{\text{exp}}$ (meV)	$E_{\text{th}}$ (meV)
(0,36)	$1.7 \pm 0.3$	<i>4</i>	$-21.3 \pm 0.8$	<i>-16</i>
(0,37)	$84.0 \pm 3.0^{\text{a}}$	<i>60</i>	$-4.7 \pm 1.4$	<i>2</i>
(1,37)	$23.0 \pm 3.0^{\text{a}}$	<i>16</i>	$10.9 \pm 1.5$	<i>18</i>
(2,37)	$1.2 \pm 0.6$	$10^{-6}$	$22.9 \pm 1.6$ $22.8 \pm 0.3^{\text{b}}$	<i>27</i>

<sup>a</sup>Reference [9].

<sup>b</sup>Reference [19].

time of flight  $t_{\text{TOF}} \in [4 \mu\text{s}, 5 \mu\text{s}]$  for  $D_2^-$  and in Fig. 9 with  $t_{\text{TOF}} \in [3.5 \mu\text{s}, 4.5 \mu\text{s}]$  for  $HD^-$ . The wide TOF interval accounts for the unknown residence time of the anions in the source prior to extraction. The branching ratio  $\beta_{v,J}$  between autodetachment and dissociation channels has been taken to be equal to 1 for all the states except for state (2,37), for which we have considered  $\beta_{2,37} \in [0.1, 0.5]$  to take into account the fact that this state decays mainly by dissociation. To reach that conclusion, we reexamined the dissociation rates observed in our previous experiment [19] while varying the beam energy from 2 to 10 keV. A fit to this rate, taking into account the linear increase of the beam intensity with the acceleration potential as expected in the absence of space charge, produces a lifetime of  $1.6 \pm 0.3 \mu\text{s}$ , fully compatible with the estimated lifetime of  $1.2 \pm 0.6 \mu\text{s}$  (see Table V).

In Tables I–VI and Figs. 1–9, we present experimental results incorporating an unforeseen long-lived state, (2,37). Remarkably, its binding energy, as determined from the detached electron energy in combination with spectroscopic data, falls in perfect agreement (see Table V) with that measured independently [19] through direct TOF analysis of its dissociation into  $D + D^-$ . Although its postulated existence resolves perfectly well the discrepancy stated in [19] regarding both its binding energy and predissociation rate, we performed an independent test based only on the present data by evaluating *Bayesian evidence* for different models including different numbers of initial states. The results are given in Fig. 10 and show that despite the increasing complexity of the model, the improvement in the goodness of fit is strong enough to provide a significant advantage to models completed with a (2,37) state, meaning that this hypothesis easily passes the Occam's-razor test.

TABLE VI. Experimental and theoretical (in italics) [10] lifetime and energy level referred to the averaged dissociation asymptote ( $H + D^-/H^- + D$ ) for experimentally accessible rovibrational states of  $HD^-$ .

$(v, J)$	$\tau_{\text{exp}}$ ( $\mu\text{s}$ )	$\tau_{\text{th}}$ ( $\mu\text{s}$ )	$E_{\text{exp}}$ (meV)	$E_{\text{th}}$ (meV)
(0,30)	$1.6 \pm 0.3$	<i>2</i>	$-6.5 \pm 1.4$	<i>1.7</i>
(1,30)	$0.8 \pm 0.2$	<i>0.6</i>	$19.0 \pm 2.3$	<i>20</i>
(0,31)	$50.7 \pm 1.0^{\text{a}}$	<i>23</i>	$14.4 \pm 1.5$	<i>22</i>

<sup>a</sup>Reference [9].

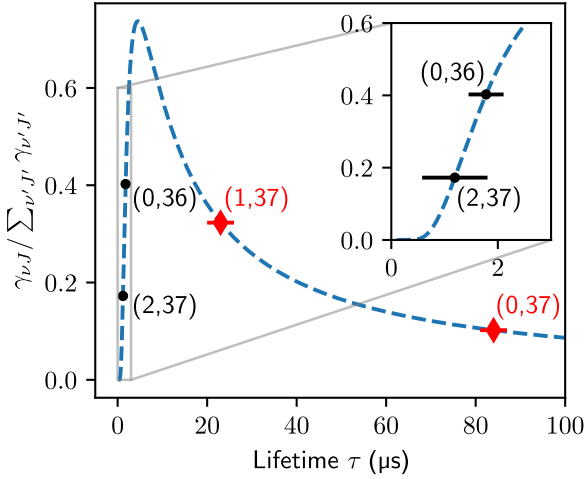


FIG. 8. Observability curve for  $D_2^-$  based on previously measured lifetimes [9] in red and presently estimated lifetimes in black. Dashed line:  $\gamma(\tau)/\sum_{\nu,J'} \gamma_{\nu,J'}$ .

To understand the presence of the (2,37) state from the perspective of the theoretical model we tested the sensitivity of the lifetime of a broad resonance seen in the  $J = 37$  partial wave in Fig. 4 on the model potential. The original intention when the model was constructed was to calculate the scattering cross sections [1,31], and the potential-energy curve for the anion [33] does not have the spectroscopic precision required here. Indeed, we see a systematic difference of 5–8 meV between theoretical and experimentally observed energies of the anion states in Tables V and VI. A correction to a fixed-nuclei potential-energy curve of similar size can be expected [42], not to mention the possible role of nonadiabatic corrections. We therefore added a negative correction to the potential of the form  $A \exp[-0.1(R - 5)^2]$  with an amplitude  $A$  in the meV range, and we repeated the analysis of the resonances in the AD cross sections. We observed a shift in the (2,37) state position and, at the same time, a narrowing of the resonance (as expected for the mechanism of tunneling

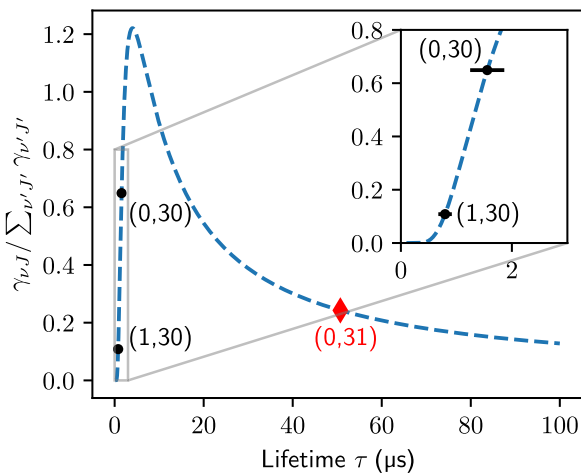


FIG. 9. Observability curve for  $HD^-$  based on previously measured lifetimes [9] in red and presently estimated lifetimes in black. Dashed line:  $\gamma(\tau)/\sum_{\nu,J'} \gamma_{\nu,J'}$ .

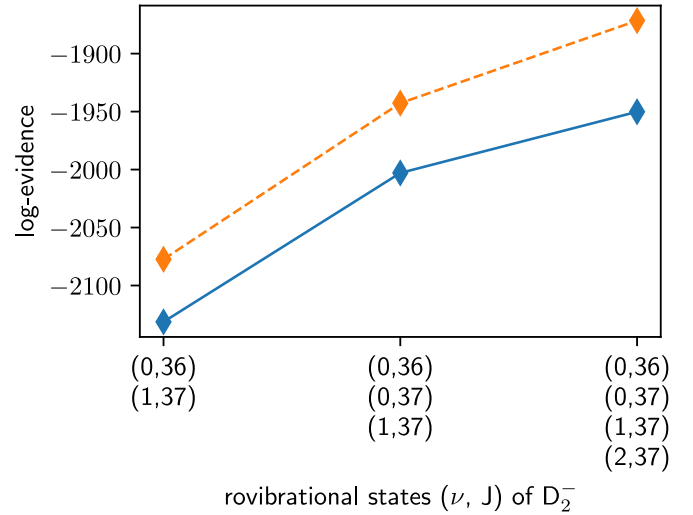


FIG. 10. Evolution of the Bayesian evidence quantity (solid line) obtained for models incorporating an increasing number of long-lived states of  $D_2^-$ . The dashed curve corresponds to the evolution of only the goodness of fit.

into the  $D + D^-$  dissociative channel). The rate of change of the lifetime of the state is quite dramatic, corresponding rather precisely to an increase of one order of magnitude with a shift in energy by  $-1$  meV. We can therefore conclude that a slight lowering of the potential is consistent with the existence of the (2,37) state observed in the experiment.

## V. CONCLUSION

We have reported an experimental determination of the autodetachment spectrum for  $D_2^-$  and  $HD^-$ . To carry out this experimental work, we used the velocity-map-imaging technique completed by a detection in coincidence of the neutral molecules produced simultaneously in order to retrieve the emission point of electrons, leading to an improvement by several orders of magnitude in the resolution of the obtained spectrum.

These results were compared to theoretical predictions in terms of both energy levels and branching ratios among the different channels, confirming the great predictive power of the present theoretical model but also revealing some limit to the description of the tunneling process through the potential barrier leading to the dissociation of the anions. This shortcoming was already raised in previous experimental work [19], but the appearance of a single kinetic-energy release in the dissociation channel could not be assigned to any rovibrational level of  $D_2^-$ .

Thanks to the very good rovibrational resolution of the spectra obtained, we provided the awaited explanation by demonstrating the existence of an additional long-lived state that is much closer to the top of the potential barrier than previously thought possible.

Experimental values for the energy levels and their estimated lifetimes were presented for both anions. Their unambiguous assignment to rotational states, which was lacking in previous experiments without resorting to theory [13–15], provides a more stringent and independent test for further theoretical developments.

## ACKNOWLEDGMENTS

The authors thank C. Lauzin for fruitful discussions on the high-resolution spectroscopy of D<sub>2</sub> and HD molecules. This work was supported by the Fonds de la Recherche Scientifique (FNRS) under IISN Grant No. 4.4504.10 and

by Czech Science Foundation Project No. 19-20524S. The authors also thank the Belgian State for the grant allocated by Royal Decree for research in the domain of controlled thermonuclear fusion. X.U. acknowledges support as a senior research associate of FNRS.

- 
- [1] H. Kreckel, H. Bruhns, M. Čížek, S. C. O. Glover, K. A. Miller, X. Urbain, and D. W. Savin, *Science* **329**, 69 (2010).
- [2] V. I. Khvostenko and V. M. Dukel'skii, *Z. Eksp. Teor. Fiz.* **34**, 1026 (1958).
- [3] R. Hurley, *Nucl. Instrum. Methods* **118**, 307 (1974).
- [4] Y. K. Bae, M. J. Coggiola, and J. R. Peterson, *Phys. Rev. A* **29**, 2888 (1984).
- [5] W. Aberth, R. Schnitzer, and M. Anbar, *Phys. Rev. Lett.* **34**, 1600 (1975).
- [6] W. Wang, A. K. Belyaev, Y. Xu, A. Zhu, C. Xiao, and X.-F. Yang, *Chem. Phys. Lett.* **377**, 512 (2003).
- [7] R. Golser, H. Gnaser, W. Kutschera, A. Priller, P. Steier, A. Wallner, M. Čížek, J. Horáček, and W. Domcke, *Phys. Rev. Lett.* **94**, 223003 (2005).
- [8] W.-G. Wang, Y. Xu, A.-M. Zhu, Z.-W. Liu, X. Liu, and X.-F. Yang, *J. Phys. B* **40**, 921 (2007).
- [9] O. Heber, R. Golser, H. Gnaser, D. Berkovits, Y. Toker, M. Erritt, M. L. Rappaport, and D. Zajfman, *Phys. Rev. A* **73**, 060501(R) (2006).
- [10] M. Čížek, J. Horáček, and W. Domcke, *Phys. Rev. A* **75**, 012507 (2007).
- [11] J. Horáček, M. Čížek, K. Houfek, P. Kolorenč, and W. Domcke, *Phys. Rev. A* **70**, 052712 (2004).
- [12] K. A. Miller, H. Bruhns, J. Eliášek, M. Čížek, H. Kreckel, X. Urbain, and D. W. Savin, *Phys. Rev. A* **84**, 052709 (2011).
- [13] L. Lammich, L. H. Andersen, G. Aravind, and H. B. Pedersen, *Phys. Rev. A* **80**, 023413 (2009).
- [14] B. Jordan-Thaden, H. Kreckel, R. Golser, D. Schwalm, M. H. Berg, H. Buhr, H. Gnaser, M. Grieser, O. Heber, M. Lange, O. Novotný, S. Novotny, H. B. Pedersen, A. Petrigani, R. Repnow, H. Rubinstein, D. Shafir, A. Wolf, and D. Zajfman, *Phys. Rev. Lett.* **107**, 193003 (2011).
- [15] P. Herwig, D. Schwalm, M. Čížek, R. Golser, M. Grieser, O. Heber, R. Repnow, A. Wolf, and H. Kreckel, *Phys. Rev. A* **87**, 062513 (2013).
- [16] A. Afaq and Du Meng-Li, *Commun. Theor. Phys.* **46**, 119 (2006).
- [17] V. Rudnev and A. G. Ureña, *Rev. Sci. Instrum.* **84**, 124102 (2013).
- [18] V. Rudnev, M. Schlösser, H. H. Telle, and Á. González Ureña, *Chem. Phys. Lett.* **639**, 41 (2015).
- [19] F. Mezdari, N. de Ruelle, and X. Urbain, *Phys. Rev. A* **96**, 032512 (2017).
- [20] M. Génévriez, K. M. Dunseath, M. Terao-Dunseath, A. Hibbert, A. Dochain, R. Marion, and X. Urbain, *Phys. Rev. A* **98**, 033410 (2018).
- [21] R. Marion, K. M. Dunseath, M. Terao-Dunseath, and X. Urbain, *Phys. Rev. A* **103**, 023115 (2021).
- [22] X. Urbain, D. Bech, J.-P. Van Roy, M. Géléoc, S. J. Weber, A. Huetz, and Y. J. Picard, *Rev. Sci. Instrum.* **86**, 023305 (2015).
- [23] B. Dick, *Phys. Chem. Chem. Phys.* **16**, 570 (2014).
- [24] G. A. Garcia, L. Nahon, and I. Powis, *Rev. Sci. Instrum.* **75**, 4989 (2004).
- [25] J. Komasa, M. Puchalski, P. Czachorowski, G. Łach, and K. Pachucki, *Phys. Rev. A* **100**, 032519 (2019).
- [26] D. Sivia and J. Skilling, *Data Analysis: A Bayesian Tutorial* (Oxford University Press, New York, 2006).
- [27] D. B. Kinghorn and L. Adamowicz, *J. Chem. Phys.* **106**, 4589 (1997).
- [28] T. F. O'Malley, *Phys. Rev.* **150**, 14 (1966).
- [29] J. N. Bardsley, *J. Phys. B* **1**, 365 (1968).
- [30] R. J. Bieniek, *J. Phys. B* **13**, 4405 (1980).
- [31] M. Čížek, J. Horáček, and W. Domcke, *J. Phys. B* **31**, 2571 (1998).
- [32] M. Berman, C. Mündel, and W. Domcke, *Phys. Rev. A* **31**, 641 (1985).
- [33] J. Senekowitsch, P. Rosmus, W. Domcke, and H.-J. Werner, *Chem. Phys. Lett.* **111**, 211 (1984).
- [34] K. A. Miller, H. Bruhns, M. Čížek, J. Eliášek, R. Cabrera-Trujillo, H. Kreckel, A. P. O'Connor, X. Urbain, and D. W. Savin, *Phys. Rev. A* **86**, 032714 (2012).
- [35] S. Roučka, D. Mulin, P. Jusko, M. Čížek, J. Eliášek, R. Plašil, D. Gerlich, and J. Glosík, *J. Phys. Chem. Lett.* **6**, 4762 (2015).
- [36] J. Horáček, M. Čížek, K. Houfek, P. Kolorenč, and W. Domcke, *Phys. Rev. A* **73**, 022701 (2006).
- [37] M. Čížek and K. Houfek, in *Low-Energy Electron Scattering from Molecules, Biomolecules and Surfaces*, edited by P. Čárský and R. Čurík (CRC Press, Boca Raton, FL, 2012), Chaps. 4–5.
- [38] R. J. Bieniek, *Phys. Rev. A* **18**, 392 (1978).
- [39] W. Domcke, *Phys. Rep.* **208**, 97 (1991).
- [40] R. J. Bieniek and A. Dalgarno, *Astrophys. J.* **228**, 635 (1979).
- [41] This symmetry is broken by nonadiabatic corrections in HD, but we neglect this effect here.
- [42] L. Pichl, *Czech. J. Phys.* **55**, 167 (2005).